TYPES OF NANO FERRITES AND THEIR CHARACTERIZATION

Shiksha Hooda

Research Scholar in Kalinga University

ABSTRACT

Powders of Mn(OH)2 and -Fe2O3 were ground together using a planetary ball mill. The activation time for the combination ranged from short to long. X-ray direction, Raman and infrared spectroscopy, scanning and transmission microscopy were used to study the soft mechanochemical process that led to the creation of the NiFe2O4 and MnFe2O4 spinel phases. In example 1, the spinel phase started forming after 4 hours of milling, whereas in case 2, it started after 3 hours of milling. In both cases, the spinel phase was completely formed after 25 hours of milling. In example (1), the nanocrystalline structure of the generated NiFe2O4 and MnFe2O4 ferrites has a crystallite size of around 30 nm, whereas in case (2), the crystallite size is approximately 40 nm. There are five Raman active modes in addition to four IR modes. The history of ferrites, as well as their characteristics, categorization methods, synthesis, and characterisation, are discussed in this article. The comparison of the four different synthesis processes, as well as the magnetic characteristics and characterisation of the ferrites, are the primary topics of this study.

keywords: *Nano Ferrites, characterization*

Introduction

Due to their high electrical resistivity, low eddy current loss, structural stability, large permeability at high frequency, high coercivity, high cubic magnetocrystalline anisotropy, good mechanical hardness, and chemical stability, nanosized spinel-type ferrites have emerged as an important class of nanomaterials in recent years. Therefore, research that focuses on the development and characterization of such nanomaterials, the development of cost-effective and environmentally friendly methods of synthesis, and the discovery of new applications for materials that are already in existence has received a significant amount of attention. Metal ferrites MFe2O4 (M = Mn2+, Co2+, Ni2+, Mg2+, Zn2+) have been pushed as an unique category of versatile nanomaterials due to the fact that their magnetic, electrical, and optical characteristics may be tuned, in addition to the fact that they have a high thermal and chemical stability. They are appropriate for a diverse array of potential applications, including photoluminescence, catalysis, photocatalysis, humidity-sensors, gas sensors, biosensors, information storage, permanent magnets, transformer cores, radiofrequency circuits, waveguide isolators, hybrid supercapacitors, ferrofluids, inductors, converters, antennas, biocompatible magnetic-fluids, magnetic drug delivery, magnetic refrigeration, microwave absorbers, water decontamination, and medical imaging, This Special Issue focuses on the synthesis and characterization of ferrite-based nanomaterials, which includes I synthesis; (ii) advanced chemical and physical characterization of structure and properties; (iii) magnetic behaviour; (iv) computational and theoretical studies of reaction mechanisms, kinetics, and thermodynamics; and (v) applications of nanomaterials in environmental, biological, catalytic, medical, cultural heritage, food,

geochemical, polymer, and materials science. It is essential for the synthesis of suitable materials for a variety of applications [8,9] to exert control over the shape and magnetic properties of ferrite nanoparticles (NPs). In this Special Issue, Duong et al. [10] reported the synthesis of $CoFe_2O_4$ NPs via a solvothermal technique employing cobalt nitrate and iron nitrate as precursors and oleic acid as a surfactant. The process was carried out using cobalt nitrate, iron nitrate, and oleic acid. In addition, the impact that the reaction duration, temperature, and oleic acid content had on the characteristics of the $CoFe_2O_4$ nanoparticles was studied. According to the findings that were gathered, the content of oleic acid plays a significant part in determining the shape as well as the characteristics of the $CoFe_2O_4$ nanoparticles. The high-quality $CoFe_2O_4$ NPs that were produced are a prospective contender for a variety of applications [10]. Some of these applications include bio-separation, magnetic resonance imaging, biosensors, drug administration, and magnetic hyperthermia. Because of its excellent stability, non-toxicity, biocompatibility, drug loading capacity, and water dispersibility, mesoporous SiO_2 improves the chemical stability of NPs, minimises the agglomeration of NPs, and enhances the stability of NPs in water, all without affecting the magnetic or dielectric properties of the NPs [1,8,9]. In this Special Issue, Dippong et al. [2] report on the effect of SiO_2 embedding on the production of single-phase ferrites, as well as on the structure, morphology, and magnetic properties of $(Zn_{0.6}Mn_{0.4}Fe_2O_4)(SiO_2)100$ (= 0–100%) NPs that were synthesised by the sol–gel method and annealed at different temperatures. These NPs were synthesised by using the According to the findings, the method of preparation has a significant amount of impact over the particle sizes, and more specifically, the magnetic properties of the NPs. At temperatures of 400, 700, and 1100 degrees Celsius, the average size of the crystallites measured between 5.3 and 27.0 nm, 13.7 and 31.1 nm, and 33.4 and 49.1 nm, respectively. The $Zn_{0.6}Mn_{0.4}Fe_2O_4$ that was embedded in SiO_2 had behaviour similar to that of a superparamagnet, but the $Zn_{0.6}Mn_{0.4}Fe_2O_4$ that was not embedded displayed the behaviour of a high-quality ferrimagnet [2]. This Special Issue also includes the research that Dumitru et al. [11] conducted on the synthesis of $Bi_2Cu(C_2O_4)_4•0.25H_2O$ by thermolysis. After that, they integrated it into a CuBi/carbon nanofiber (CNF) paste electrode and used it for the electrochemical detection of amoxicillin (AMX) in aqueous solution. The findings that were obtained suggested that an AMX detection in aqueous solutions might be accomplished with the use of a CuBi/CNF paste electrode. The selective and simultaneous detection of AMX in a multi-component matrix is also conceivable if the detection technique includes a concentration step [11]. This is accomplished by adding a concentration step.

What is Nanoferrite

According to O'Connor (1999), ferrite is a significant class of materials that have the potential to be utilised in integrated circuits, transformer cores, and magnetic recording. Because ferrites possess unusual features and may be used in a variety of technological applications, the study of ferrites has garnered a significant amount of interest from the scientific community. This is particularly true as the size of the particles reaches the nanoscale scale.

Research is being conducted in many different sectors, including physics, chemistry, the medical sciences, and material engineering. One of the areas that is seeing the most activity is the study of nano-crystalline materials. In today's world, research in the field of material science is focused on developing new materials that have improved qualities as well as unique methods of synthesis in order to keep up with the ever-increasing demand from the technological industry. When compared with their bulk counterparts, ferrite nanoparticles have fundamentally different magnetic and electrical characteristics, which makes the

study of these nanoparticles an interesting area of research. When compared to their comparable conventional oxides, nano-oxides have been discovered to be superior catalysts due to the unique electrical characteristics that they possess (Willard et al. 2004).

Nanomaterials are now the focus of much study because of the vast number of uses that can be found for them and the intriguing features that they possess. Ferrites are a family of ferromagnetic compounds that often make use of magnetic nanoparticles. Their chemical formula is $M Fe_2O_4$, where M can represent any one of various divalent metallic elements such as Mg, Fe, Co, Ni, Cu, etc. Nanoferrites have emerged as an important topic of discussion in contemporary scientific study, both from the point of view of their synthesis and their potential applications. The manner in which nanoferrites are prepared as well as the sintering environment both have a significant impact on their characteristics. Because of this, acquiring ferrites of a good quality relies heavily on making the right choice when it comes to the production method. The production of a variety of nanoparticles using the sol-gel auto-combustion approach, in particular ferrites, has shown that the particle size, size distribution (Sugimoto 1999; Suzuki 2001; Nayak and Jena 2014), chemical stoichiometry, and cation occupancy can all be controlled.

Crystal Structure of Ferrites

Crystal structure and chemical compositions being the basis, ferrites are divided into three different types: (i) Spinel Ferrites, (ii) Garnets, and (iii) Hexaferrites.

Spinel Ferrites

Spinel ferrites have the general formula MFe_2O_4 or AB_2O_4 (where M or A is divalent metal cations such as Co^{2+}, Ni^{2+}, Zn^{2+}, etc., and B is Fe^{3+}), and they belong to the space group Fd3m. This space group is derived from the crystal structure of the natural mineral spinel, which is $MgAl_2O_4$, where M is divalent metal cations such as Fe^{2+}, Mn^{2+}, Co2 (Gopalan and Anantharaman 2009). In Figure .1 (Issa et al. 2013), we see a representation of the crystal lattice structure of spinel ferrites. In spinel ferrites, a unit cell with a face-centered cubic (FCC) structural arrangement is formed by 32 oxygen atoms. This leaves two different kinds of sites: tetrahedral sites (A) and octahedral sites (B), each of which is surrounded by four or six oxygen atoms, depending on the kind of site. Spinel ferrites have an FCC crystal structure that consists of 64 tetrahedral sites and 32 octahedral sites (B). In a unit cell, the cations take up one-eighth of the tetrahedral sites (A) and one-half of the octahedral sites (B) such that the lattice does not lose its electrical neutrality. This is done so that the octahedral sites (B) remain unoccupied. Spinel ferrites have a crystal structure with eight molecules packed into each unit cell of the formula (Sugimoto 1999). Spinel ferrites may be broken down into three different groups based on the distribution of cations in tetrahedral (A) and octahedral (B) sites. These categories include normal spinel, inverse spinel, and mixed spinel ferrite structure. Tetrahedral sites are present when.

○ Oxygen   ◉ B-atoms octahedral sites

● A-atoms tetrahedral sites
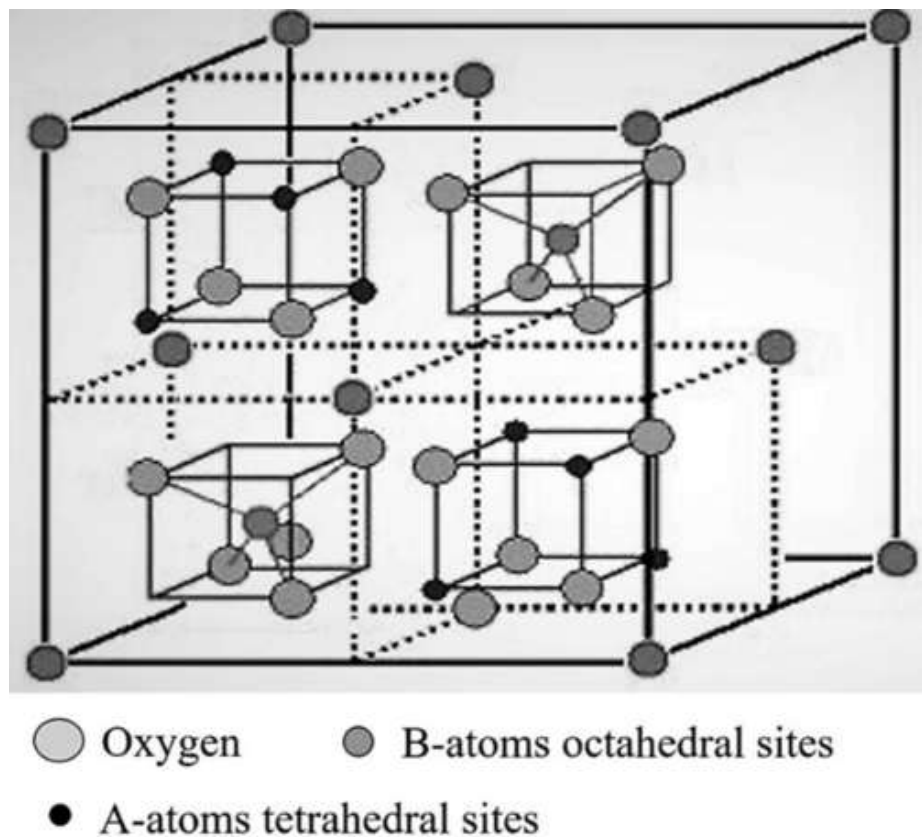
AB_2O_4 **spinel** The black cubes are also contained in the back half of the unit cell

Figure: 1 Crystal structure of spinel ferrites (Issa et al. 2013).

(A) are occupied by divalent metal cations and octahedral sites

(B) if the vacancies in the structure are filled by cations of three different types of metal, then the structure is referred to as normal spinel. The formula (Ml-5Fe6) A [M6Fe2-6] B 04 is used to define normal spinel ferrites. In this formula, the first term in brackets describes the tetrahedral (A) sites components, and the second term in square brackets describes the octahedral (B) sites components. The number 6 represents the degree of inversion parameter of cations that have zero values. One example of a typical spinel ferrite is the compound ZnFe204. In a system known as an inverted spinel ferrite, all of the divalent cations are spread over tetrahedral (A) sites, while the trivalent cations are scattered over tetrahedral (B) sites. The remaining octahedral sites contain the remaining trivalent cations. In inverted spinel ferrites, the value of 6 is equal to one, while in mixed spinel ferrites, the value of 6 may be expressed as $0 + 5 + 1$ (Harris et al. 1996; Sickafus and Hughes 1999).

Garnet Ferrites

The garnet crystals that make up garnet ferrites have a crystal structure that looks like this: $Mn_3Al_2Si_3O_{12}$. In order to produce garnet ferrites, Al and Si are first exchanged for Fe^{5+} ions, and then Mn is switched out for a rare earth cation (R). This results in the formation of a magnetic garnet with the general formula $R_3^{3+}Fe_5^{3+}O_{12}$. The garnet ferrite has a structure that is body-centered cubic, and there are eight formula units in total. The garnet ferrites crystal has cubic symmetry and is composed of three sub-lattices. These sub-lattices each contain 24 tetrahedral (A), 16 octahedral (B), and 24 dodecahedral (C) sites, respectively. Rare earth cations, such as Y, La, Er, Gd, Sm, and Eu, occupy the biggest dodecahedral sites, whereas Fe^{3+} cations fill the tetrahedral (A) and octahedral (B) sites in the structure.

Hexagonal Ferrites

Hexagonal ferrites and the identification of their magnetic properties were initially accomplished by Went, Rathenau, Gorter, Van Oostershout, Jonker, and Wijn. Braun also contributed to this endeavour (Zijlstra 1982). Permanent magnets belonging to the class known as hexagonal ferrites have the general formula MFe_2O_{19}, where M can be any one of the elements Ba, Sr, Ca, or Pb. The hexagonal ferrites have a crystal structure that is created by oxygen ions that have a close-packed hexagonal arrangement unit cell that comprises two molecules of $MFe_{12}O_{19}$. Because hexagonal ferrites have such a high magneto-crystalline anisotropy energy and coercivity, it is conceivable for them to be used to create a permanent magnet. On the basis of the chemical formula and the crystal structure, they are classified into the following five groups: M-type, also known as $SrFe_{12}O_{19}$; W-type, also known as $SrMe_2Fe_{16}O_{27}$; Y-type, also known as $SrMe_2Fe_{12}O_{22}$; X-type, also known as Sr,Me,Fe_2sO_{46}; and Z-type, also known as $Sr_2Me_2Fe_{24}O_4$, also known as Sr_2M.

Properties of Nanoferrites

The characteristics of magnetic nanoparticles are determined by the particle size, the surface effect, the distribution of cations in tetrahedral (A) and octahedral (B) sites, the methods of synthesis, the amount and kinds of dopant, and the annealing temperature. Due to a rise in the surface-to-volume ratio of atoms in particles, there is a considerable change in the system's physical, chemical, and mechanical characteristics as the particle size drops from a bulk range to a nanoscale range. This is the source of the major change (Mathew and Juang 2007; William and Rethwisch 2012). When compared to those of a bulk specimen, the magnetic characteristics of a nanoparticle system, such as magnetic moment or magnetization, and magnetic anisotropy, are distinct from those of the bulk specimen (Stoner and Wohlfarth 1948). A few microns to a few nanometers is the size range in which the size-dependent magnetic characteristics of magnetic materials may be measured. In bulk form, particles exist in a multi-domain structure. When taken by itself, a domain is the region where all of the spins' magnetic moments of atoms are aligned in a certain direction, resulting in uniform magnetization as a result of this alignment. The moment of domain walls is what allows the magnetization of the multi-domain structure to be switched around. The domain barriers of the system become energetically unfavourable as the particle size drops below the nanometer range. This results in the development of a single domain state in which all of the spins' moments are aligned in the same direction. A super exchange interaction is another factor that determines how the spinel ferrite nanoparticles will behave at the Curie temperature. The value of the Curie temperature is said to increase in proportion to the strength of the super exchange interaction. Due to the substantial features that they possess, spinel ferrites become excellent candidates for application in the commercial sector. Spinel ferrites are an intriguing possibility for use in electronic and magnetic device applications due to their one-of-a-kind properties, which include high magnetic permeability, high thermal stability, high electrical resistivity, high electrolytic activity, high electrolytic activity, low magnetic losses, and

resistance to corrosion (Olsen and Thonstad 1999; Suzuki et al. 2001). The distribution of cations in distinct lattices that have varied ionic radii, the composition of the spinel type ferrite nanoparticles, and the process by which they were synthesised all have an impact on the chemical, structural, electrical, and magnetic characteristics of the nanoparticles (Gubbala et al. 2004).

Experimental

The following crystalline powders were utilised as starting materials: (1) manganese(II)-hydroxide (Mn(OH)2, Merck 95% purity) and hematite (-Fe2O3, Merck 99% purity); and (2) nickel(II)-hydroxide (Ni(OH)2, Merck 95% purity) and hematite (-Fe2O3, Merck 99% purity). In a planetary ball mill operating in the air environment, a soft mechanochemical synthesis was carried out (Fritsch Pulverisette 5). All of the samples were prepared and milled individually, and each one had a unique beginning composition as well as a unique milling time. After the predetermined milling durations had elapsed (4, 10, and 25 hours for case 1), and 3, 12, and 25 hours for case 2), the mill was stopped, and a little amount of powder was extracted from the vial for analysis. A characterization of the samples that were acquired was accomplished by:

Analyses of the X-ray direction (XRD) were performed on powders that had been subjected to varying amounts of milling times using a Philips PW 1050 diffractometer that was fitted with a PW 1730 generator (40 kV 20 mA) while employing nickel-altered Cu K radiation at room temperature. The measurements were taken in a range of two degrees, from ten to eighty, with a scanning step width of 0.05 degrees and a scanning period of ten seconds for each step. Following the completion of the XRD analysis, the powder was reintroduced into the vial in order to recreate the original grinding conditions (balls to powder weight ratio).

The Jobin Ivon T64000 monochromator was utilised in the process of carrying out the Raman measurements of the combination powders. In order to concentrate the 514 nm light that was produced by a Coherent Innova 99 Ar+ laser on the specimen, an optical microscope equipped with a 100x objective was utilised. The backscattered radiation was collected using the same microscope as the original sample. A charge-coupled device (CCD) detection system was able to detect the light that was scattered as a result of the scattering. The Raman spectra at room temperature have a wavelength range that is between 100 and 800 cm-1. The sample had an average power density of 20 milliwatts per millimetre squared.

The BOMMEM DA-8 FIR spectrometer was utilised in order to carry out the infrared (IR) measurements. For the purpose of covering the wave number range from 50 to 700 cm-1, a DTGS pyroelectric detector was utilised.

Both scanning electron microscopy (SEM, Model TESCAN Vega TS130MM) and transmission electron microscopy were utilised in order to investigate the morphology of powders as well as the size of soft mechano-synthesized ferrite crystallites (200 kV TEM, Model JEM-2100 UHR, Jeol Inc., Tokyo, Japan).

In order to get the Mossbauer spectra of powder samples, measurements were performed at room temperature (RT) with a source of 57Co in Rh (1.85 GBq). The trials were carried out using a transmission geometry that was standard, and the acceleration was held constant throughout the calibration process using the laser spectrum. The application known as The WinNormos Site performed an analysis on the data. Transmission integral was utilised in order to effect corrections to the sample thickness.

Results and discussion

Under air conditions, we also carried out soft mechanochemical synthesis and mechanical milling of (1) $Ni(OH)_2$ + Fe_2O_3 $NiFe_2O_4$ + H_2O and (2) $Mn(OH)_2$ + Fe_2O_3 $MnFe_2O_4$ + H_2O. Both of these reactions led to the formation of $NiFe_2O_4$ and $MnFe_2O_4$, respectively. The X-ray diffraction patterns of stoichiometric mixes of powdered reactants $Ni(OH)_2$ and $-Fe_2O_3$ that were ground in a ball mill for different amounts of time are depicted in Figure 1a (4, 10, and 25 h). Di raction peaks corresponding to crystalline $Ni(OH)_2$ (JCPDS card 74-2075), NiO (JCPDS card 89-5881), NiOOH (JCPDS card 27-0956), $-Fe_2O_3$ (JCPDS card 89-8104), FeO(OH) (JCPDS card 89-6096), and $NiFe_2O_4$ can be identified in the XRD pattern of the initial powder (JCPDS card 89- -4927). By increasing the milling time, it is possible to see that the primary peaks for the hematite phase, which are located at 2 = 35.6 and 33.15, have been continually lowered (Fig. 2a). It is possible to see $Ni(OH)_2$ peaks that are nearly gone and $-Fe_2O_3$ peaks that are somewhat broader but have a lower strength. It is essential to take notice of the fact that during the milling of powder mixes between 4 and 10 hours, a phase known as FeO(OH) (JCPDS card 89-6096) as well as NiO (JCPDS card 89-5881) might appear. The primary reason for this phenomenon is that powder Fe_2O_3 in an atmosphere that is wet and heated by intensive milling reacts with water, and $Ni(OH)_2$ quickly decomposes through the reaction $Ni(OH)_2$ NiO + H_2O. As a result, there is a negligible number of peaks that correspond to the starting compound $Ni(OH)_2$ after 4 hours of milling (Fig. 2a), which indicates that the phenomenon is caused by this reaction. Continued milling for up to 25 hours results in the complete synthesis of the next phase. All eight of the pattern's diffraction peaks (18.4, 30.1, 35.6, 37.3, 43.4, 57.4, and 62.8) are well indexed as the cubic spinel phase with the fcc structure after 25 hours of milling time (fcc face cubic centered). The spinel cubic structure of $NiFe_2O_4$ may be deduced from the fact that the diffractogram displays several different reflection planes with indexes such as (k h l) (111), (220), (311), (222), (400), and (511) and (440).
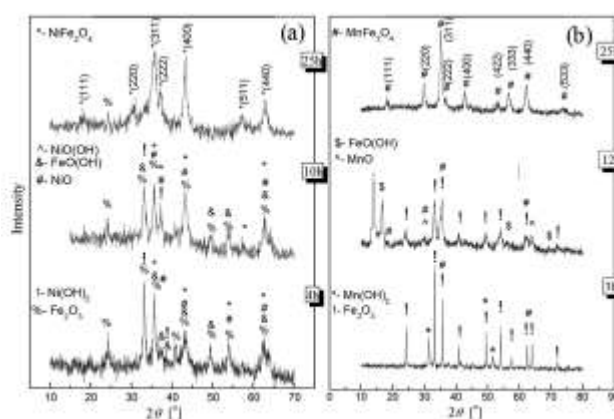
Fig. 2. X-ray diraction pattern of the mixture of (a) Ni(OH)2 and α-Fe2O3 and (b) Mn(OH)2 and αFe2O3 powders after various milling times.

The X-ray diffraction patterns of a combination of $Mn(OH)_2$ and $-Fe_2O_3$ powders that have been mechanochemically activated for various milling periods are depicted in Figure 2b (3, 12, and 25 h). Sharp di raction peaks can be seen in the XRD pattern of the initial powder, which correspond to crystalline $Mn(OH)_2$ (JCPDS card 73-1133) and $-Fe_2O_3$ (JCPDS card 89-8103) [19]. These peaks can be seen in the XRD pattern. The dispersion peaks that correspond to the simple oxide and hydroxide progressively diminish as the milling duration increases. In the spectrum, each and every one of the peaks that are

unique to Mn(OH)2 and -Fe2O3 can be easily identified (Fig. 1b). The XRD pattern shows that during the mechanochemical treatment that lasted for three hours, only the sharp peaks that resulted from the well-crystallized Mn(OH)2 and -Fe2O3 were present. During the milling of powder mixes for 3 to 12 hours, the novel phases of FeO(OH) (JCPDS card 89-6096) and MnO (JCPDS card 75-1090) arise. These phases may be identified by their respective JCPDS cards. It is well knowledge that the grinding process causes the container to get overheated, which, at temperatures higher than 100 degrees Celsius, results in the formation of water vapour. When the container is opened, there is some water that is lost through evaporation. It's important to keep in mind that the hydroxides will eventually turn into oxides. At the same time, the peaks that are typical of hydroxide and oxide may be seen in the data (Fig. 1b). It's possible that this happened as a result of the milling vessel being opened. The explanation for this is nearly the same for all of the samples that were obtained after milling the powder combination for a period of 12 hours. This indicates that there will be no additional grinding up to 12 hours, which will result in the completion of the new phase's synthesis. The creation of a new phase of MnFe2O4 is clearly shown by the presence of a new peak at 2 = 18.09, 29.89, 35.37, 42.85, 53.11, 56.76, and 62.13 and 73.74 (JCPDS card 74-2403). (Fig. 1b). The peaks are effectively indexed to the crystal plane of spinel ferrite (k h l), namely at the coordinates (111), (220), (311), (400), (333), (440), and (533), respectively. The results of this study confirm that the mechanochemical synthesis of MnFe2O4 is both realisable and successful after a milling time of 25 hours. With the use of Scherrer's relation [20], we were able to compute the crystallite size D of NiFe2O4 and MnFe2O4 powders by utilising the whole width at half maximum of the XRD peaks:

$$D = 0.9\lambda/(\beta \cos \theta),$$

where D is the grain size of the crystallites, = 1.5406 is the wavelength of the Cu K, and is the broadening of the diffraction line as measured at half its maximum intensity (radians). NiFe2O4 has a crystallite size of 30 nm, while MnFe2O4 has a crystallite size of 40 nm, according to the results of the (311) experiments that produced the strongest reflections. The most helpful way of investigation for detecting the crystalline structure of materials is called X-ray diffraction (XRD). However, XRD analysis of nanocrystalline materials does not offer sufficient intensity of the essential diffraction peaks to obtain the whole crystallographic information. This is a limitation of the technique. In order to achieve a structure analysis of nanocrystalline materials, additional methods such as Raman and IR analysis are required. This is necessary in order to differentiate between MFe2O4 (M = Mn, Co, Ni, Cu, Zn, Mg, Cd, etc.) and Fe3O4 or -Fe2O3 (possible impurity phases) with similar structure elements and, as a result, similar XRD patterns. Raman and IR analysis are examples of Spinel is the crystal structure of M2+Fe3+ 2O 2 4 (space group Fd3m), where the lattice of O2 ions produces tetrahedral (A-sites) and octahedral (B-sites) local symmetry. M2+ can either be Mn or Ni. In a typical spinel crystal structure, the only sites occupied by divalent M2+ ions are A, while the only sites occupied by trivalent Fe3+ ions are B. Ions with divalent charges fill up fifty percent of the spinel's B sites, whereas ions with trivalent charges fill up the remaining B sites and all of the spinel's A sites. According to group theory, the structure of a spinel should exhibit five Raman active modes: A1g +Eg + 3F2g and four F1u infrared active. The crystal structure of NiFe2O4 is (mainly) an inverted spinel. The five Raman peaks in NiFe2O4 are all asymmetric, with shoulders on the high energy and low energy sides respectively. Every peak has the potential to be displayed as a double. The existence of non-equivalent atoms at the B-sites is responsible for the appearance of additional peaks (but with structural ordering over B-sites). When viewed on a microscopic scale, the structure of NiFe2O4 may be thought of as a combination of two sublattices containing Fe3+ and Ni2+ ions. Asymmetry in nanocrystalline samples can be attributed in part to the configuration of nanoparticles

as well as their size distribution. It has been demonstrated that the structure of NiFe2O4 is influenced by the circumstances under which it is synthesised. It is possible to describe NiFe2O4 as a blend of regular spinel ferrite and inverse spinel ferrite. The structure shifts from a pure normal spinel structure to a mixed spinel structure as the calcination temperature or milling time is increased. Additionally, single wide bands in the Raman spectra become asymmetric and take on a double peak-like shape.

It is possible to draw the conclusion that the spinel structure of these samples is generally normal based on the fact that the Raman spectra of MnFe2O4 nanocrystalline samples generated by the mechanochemical process at low temperature have virtually any apparent doublet structure.
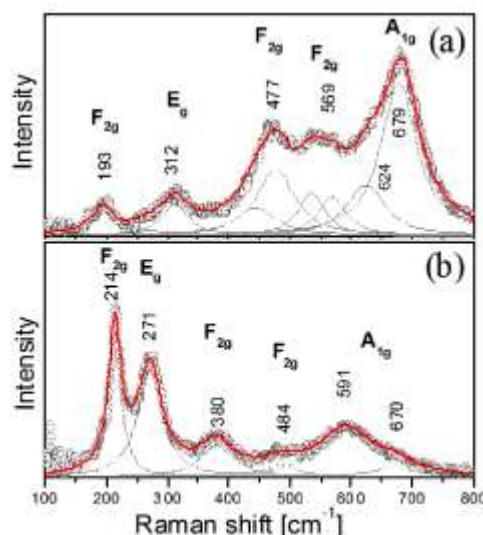
Fig. 3. Raman spectra at room temperature of the mixture of: (a) Ni(OH)2 and α-Fe2O3 and (b) Mn(OH)2 and α-Fe2O3 powders after 25 h milling time.

After 25 hours of mixing, the Raman spectra of samples generated by mixing (1) Ni(OH)2 and -Fe2O3 and (2) Mn(OH)2 and -Fe2O3 are analysed by deconvolution (Fig. 3), and modes are assigned, as is customary. The modes that occur above 600 cm1 in cubic ferrites mostly correspond to the motion of oxygen in tetrahedral AO4 groups; consequently, the mode that occurs at 679 cm1 for NiFe2O4 and the dublet modes that occur at 591 670 cm1 for MnFe2O4 can be considered as Ag symmetry with some degree of plausibility. The properties of the octahedral sites are reflected in the behaviour of the other low-frequency modes (BO6). The mode that was detected at approximately 679 cm1 for NiFe2O4 and 591 670 cm1 for MnFe2O4 may be ascribed to tetrahedral Ni2+ and Mn2+ stretching. Additionally, the band that was observed at 477 cm1 and 484 cm1 involves the Fe3+ vibration at the octahedral site in both instances. The broad features are displayed by the five first-order Raman modes at about 193, 312, 477, 599, and 679 cm1 (Fig. 3a) and 214, 271, 380, 484, and 591 670 cm1. The symmetry type F2g is represented by the three modes that were found to be around 193, 477, and 599 cm-1 for NiFe2O4 and 214, 380, and 484 cm-1 for MnFe2O4, respectively. Additionally, it is possible to show that the modes 312 and 271 cm1 correspond to the same symmetry Eg for the respective compounds NiFe2O4 and MnFe2O4, respectively. Infrared spectra were obtained in the range of 50–700 cm–1 for the purpose of further characterising the NiFe2O4 and MnFe2O4 ferrites that were produced (Fig. 3). The spectral characteristics F1u(3) and F1u(4), which are the most prominent, correspond to the vibrations of positive ions in NiFe2O4 and MnFe2O4, respectively, at octahedral and tetrahedral sites. It is well knowledge that the band with a

frequency of 700 cm1 is associated with the inherent vibrations of the tetrahedral site, whereas the band with a frequency of 400 cm1 is thought to be associated with the vibrations of the octahedral site. The reason for the different values of the energy location for these modes is that the octahedral and tetrahedral sites have different values for the distance between the metal ions and O2. It is possible to see the $NiFe_2O_4$ TO LO splitting of the F1u(4) IR mode in its reflectivity spectrum.
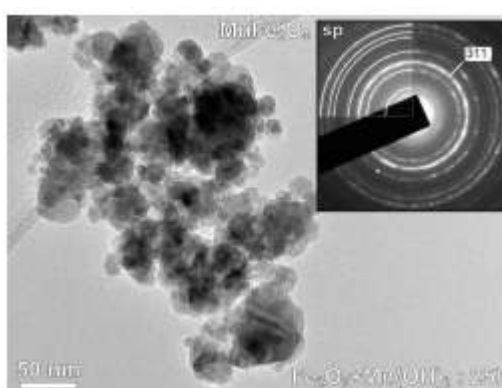

Fig. 4. IR spectra at room temperature of the mixture of: (a) Ni(OH)2 and α-Fe2O3 and (b) Mn(OH)2 and α-Fe2O3 powders after 25 h milling time.
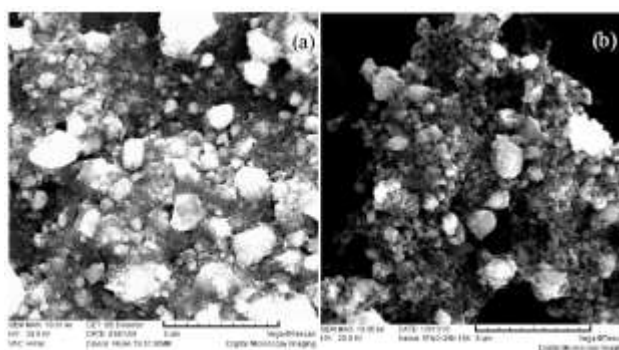

Fig. 5. SEM images of nanoscale of mechanosynthesized (a) NiFe2O4 and (b) MnFe2O4 powders after 25 h of milling time.

After 25 hours of mixing, the Raman spectra of samples generated by mixing (1) Ni(OH)2 and -Fe2O3 and (2) Mn(OH)2 and -Fe2O3 are analysed by deconvolution (Fig. 5), and modes are assigned, as is customary. The modes that occur above 600 cm1 in cubic ferrites mostly correspond to the motion of oxygen in tetrahedral AO4 groups; consequently, the mode that occurs at 679 cm1 for NiFe2O4 and the dublet modes that occur at 591 670 cm1 for MnFe2O4 can be considered as Ag symmetry with some degree of plausibility. The properties of the octahedral sites are reflected in the behaviour of the other low-frequency modes (BO6). The mode that was detected at approximately 679 cm1 for NiFe2O4 and 591 670 cm1 for MnFe2O4 may be ascribed to tetrahedral Ni2+ and Mn2+ stretching. Additionally, the band that was observed at 477 cm1 and 484 cm1 involves the Fe3+ vibration at the octahedral site in both instances. The broad features are displayed by the five first-order Raman modes at about 193, 312, 477, 599, and 679

cm1 (Fig. 5a) and 214, 271, 380, 484, and 591 670 cm1. The symmetry type F2g is represented by the three modes that were found to be around 193, 477, and 599 cm-1 for NiFe2O4 and 214, 380, and 484 cm-1 for MnFe2O4, respectively. Additionally, it is possible to show that the modes 312 and 271 cm1 correspond to the same symmetry Eg for the respective compounds NiFe2O4 and MnFe2O4, respectively. Infrared spectra were obtained in the range of 50–700 cm–1 for the purpose of further characterising the NiFe2O4 and MnFe2O4 ferrites that were produced (Fig. 6). The spectral characteristics F1u(3) and F1u(4), which are the most prominent, correspond to the vibrations of positive ions in NiFe2O4 and MnFe2O4, respectively, at octahedral and tetrahedral sites. It is well knowledge that the band with a frequency of 700 cm1 is associated with the inherent vibrations of the tetrahedral site, whereas the band with a frequency of 400 cm1 is thought to be associated with the vibrations of the octahedral site. The reason for the different values of the energy location for these modes is that the octahedral and tetrahedral sites have different values for the distance between the metal ions and O2. It is possible to see the NiFe2O4 TO LO splitting of the F1u(4) IR mode in its reflectivity spectrum.

Fig. 6. TEM image with corresponding EDP of Mn(OH)2 and α-Fe2O3 after milling for 25 h. Spinel- -type reections dominate the diraction pattern (inset).
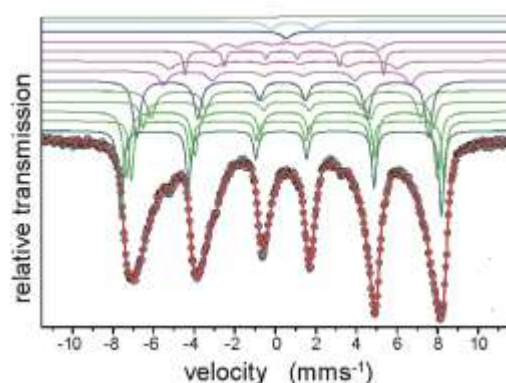
Fig. 7. Mössbauer spectra at room temperature of the mixture of Mn(OH)2 and α-Fe2O3 powders after 25 h milling time.

Figure 7 displays two Mossbauer spectra for samples that were produced at room temperature from the combination of (1) Ni(OH)2 and -Fe2O3 powders and (2) Mn(OH)2 and -Fe2O3 powders following a milling duration of 25 hours. Both sets of samples were milled for 25 hours. Both of these samples have a total of twelve subspectra that make up their Mossbauer spectra. In accordance with the sizes of the particles, they are categorised into one of three classes. When describing the cation distribution at the mixed spinel (MnxFe1x) T(Mn1xFe1+x) MO4, one needs ve subspectra for a big nanoparticle. The first

sextet is associated with the ferric ion at the tetrahedral site T, which belongs to the cubic point symmetry group Td. It has been confirmed with a quadrupole splitting of zero. As a consequence of the superexchange connection mediated by oxygen ions, the antiferromagnetic hyperne interaction felt by the cations at this location is the most potent. Because of the distinct nature of the surrounding environment, the ferric ions that are located at the octahedral coordination site (M) display four sextets. The distribution of cations at the (T) site has a significant impact on the ferric cations that are found at the (M) location [17]. As a consequence of this, the line widths of the associated sextets have increased. Due to the fact that the octahedral site belongs to the D3d group of trigonal point symmetry, one might anticipate a particular electric field gradient (EFG). The magnitude of the hyperne induction is proportional to the separation of the magnetic ions as well as the angle formed by the FeOFe bonds. In addition, the volume of the particles has an effect on the strength of the material. As a direct result of the superparamagnetic relaxation effect taking place at very tiny nanoparticles, we are no longer in a position to see a sextet. It has been discovered that both a singlet and a doublet are shown, with the octahedral and tetrahedral coordinations, respectively, being responsible for their formation. When the size of the particles is tiny as well, the preference for the cation site is affected. As the size of the particles reduced, we observed that the quantity of $Mn2+$ at the tetrahedral site dropped from 76% to 51% in the first sample that we received from the mixture of $Mn(OH)2$ and $-Fe2O3$ powders after 25 hours of milling time. This was discovered in the first sample that we obtained. The quantitative examination of the Mossbauer spectra of the examined nanocrystalline ferrites that were generated by mechanochemical treatment established that $NiFe2O4$ possesses an inverse spinel structure, whereas $MnFe2O4$ had a mixed, largely normal spinel structure.

Conclusions

We show in this study that it is feasible to create $NiFe2O4$ and $MnFe2O4$ ferrites by soft mechanochemical synthesis beginning with the mixture of (1) $Ni(OH)2$ and $-Fe2O3$ powders and (2) $Mn(OH)2$ and $-Fe2O3$ powders. Both of these mixtures begin with powders that have been ground into a powder form. It has been demonstrated that the mechanochemical treatment of mixtures containing starting materials leads to the amorphization of the starting powders. This results in the formation of the phase of $Ni(OH)2$, NiO, $NiO(OH)$, $FeO(OH)$, and $Fe2O3$ after 4 h and 10 h of milling, and only the $NiFe2O4$ phase after 25 h, respectively (case 1). In contrast, when case (2) is seen, $Mn(OH)2$ and $Fe2O3$ phases appear after three hours of milling, followed by $Fe2O3$, MnO, and $FeO(OH)$ phases after twelve hours, and finally, after twenty-five hours, only the $MnFe2O4$ phase is observed. Research conducted using the Raman spectrometer has revealed the existence of first-order Raman active modes. In the production of $NiFe2O4$ and $MnFe2O4$ ferrite phases, the strength of the Raman and IR modes is relatively low. This is to be anticipated for nanocrystalline materials.

References

1. Adam JD, Davis LE, Dionne GF, et al. (2002) Ferrite devices and materials. IEEE T Microw Theory 50: 721–737.
2. S.S.P. Parkin, M. Hayashi, L. Thomas, Science 320, 190 (2008).
3. S. Mornet, S. Vasseur, F. Grasset, P. Veverka, G. Goglio, A. Demourgues, J. Portier, E. Pollert, E. Dugust, Prog. Solid State Chem. 34, 237 (2006).
4. D.L. Zhao, X.W. Zeng, Q.S. Xia, J.T. Tang, J. Alloys Comp. 469, 215 (2009).
5. J.P. Fortin, F. Gazeau, C. Wilhelm, Eur. Biophys. J. 37, 223 (2008).
6. C.S. Gill, W. Long, C.W. Jones, Catal. Lett. 131, 425 (2009).

7. V. ' epelák, I. Bergmann, A. Feldho, P. Heitjans, F. Krumeich, D. Menzel, F.J. Litterst, S.J. Campbell, K.D. Becker, J. Phys. Chem. C 111, 5026 (2007).

8. L. Wang, J. Ren, Y. Wang, X. Liu, Y. Wang, J. Alloys Comp. 490, 656 (2010). [

9. A. Baykal, N. Kasapo§lu, Y. Köseo§lu, M.S. Toprak, H. Bayrakdar, J. Alloys Comp. 464, 514 (2008).

10. Pullar RC (2012) Hexagonal ferrites: A review of the synthesis, properties and applications of hexaferrite ceramics. Prog Mater Sci 57: 1191–1334.

11. Dairy ARA, Al-Hmoud LA, Khatatbeh HA (2019) Magnetic and structural properties of barium hexaferrite nanoparticles doped with titanium. Symmetry 11: 732.

12. Snelling EC (1988) Soft Ferrites, Properties and Applications, Butterworth-Heinemann Ltd.

13. Smit J, Wijn HPJ (1959) Ferrites, Eindhoven: Philips Technical Library, 150.

14. Issa B, Obaidat I, Albiss B, et al. (2013) Magnetic nanoparticles: Surface effects and properties related to biomedicine applications. Int J Mol Sci 14: 21266–21305.

15. Ammar S, Helfen A, Jouini N, et al. (2001) Magnetic properties of ultrafine cobalt ferrite particles synthesized by hydrolysis in a polyol medium. J Mater Chem 11: 186–192.

16. Šutka A, Gross KA (2016) Spinel ferrite oxide semiconductor gas sensors. Sensor Actuat BChem 222: 95–105.

17. Veena M, Somashekarappa A, Shankaramurthy GJ, et al. (2016) Effect of 60Co gamma irradiation on dielectric and complex impedance properties of Dy3+ substituted Ni–Zn nanoferrites. J Magn Magn Mater 419: 375–385.

18. Krishnan V, Selvan RK, Augustin CO, et al. (2007) EXAFS and XANES investigations of CuFe2O4 Nanoparticles and CuFe2O4–MO2 (M = Sn, Ce) Nanocomposites. J Phys Chem C 111: 16724–16733.